A Multistatic Uniform Diffraction Tomography Algorithm for Microwave Imaging in Multilayered Media for Microwave Drying

Adel Omrani, Rahul Yadav, Guido Link, and John Jelonnek

Abstract—Microwave tomography (MWT) based control is a novel idea in industrial heating systems that demands fast DAQ and real-time imaging algorithms. Uniform diffraction tomography (UDT) is one such technique that can provide real-time imaging. However, its single-input single-output data based inverse scattering formulation can lead to time-consuming DAQ. In this article, a multistatic uniform diffraction tomography (MUDT) imaging algorithm is proposed for a fixed array MWT system. The MWT system is integrated into the industrial heating unit HEPHAISTOS to estimate the moisture distribution in a polymer foam. In addition, a technique is presented to retrieve the electrical properties of the targets using reconstructed information from MUDT and by investigating the singular values of multistatic scattering data. Through numerical and experimental data for the considered moisture scenarios, the MUDT approach is tested, and its comparison with the UDT approach is shown. Reconstructed results show that in comparison to UDT, the MUDT approach i) eliminates the need for mechanical scanning, ii) provides aliasing-free images by following Nyquist sampling criteria, and iii) can resolve multiple targets in the imaging media with significant improvement in the spatial resolution that further augments in the correct retrieval of the dielectric constants of the target.

Index Terms—industrial drying, multilayered media, microwave tomography, multistatic uniform diffraction tomography

I. INTRODUCTION

INDUSTRIAL applications of microwave tomography (MWT) have been rapidly increasing in a wide range of areas for inspection, monitoring purposes, quality control of the product, and safety issues, to name a few [1]–[3]. A novel idea is to apply tomography-based control (TOMOCON) by integrating MWT with the control unit of the high power industrial microwave drying system called HEPHAISTOS [4]

Adel Omrani is is with the Institute for Pulsed Power and Microwave Technology, Karlsruhe Institute of Technology, Karlsruhe, Germany(email: adel.hamzekalaei@kit.edu).

Rahul Yadav is with the Department of Applied Physics, University of Eastern Finland, Kuopio, Finland (e-mail: rahuly@uef.fi).

Guido Link is with the Institute for Pulsed Power and Microwave Technology, Karlsruhe Institute of Technology, Karlsruhe, Germany (e-mail: guido.link@kit.edu).

John Jelonnek is with the Institute for Pulsed Power and Microwave Technology; and Institute of Radio Frequency Engineering and Electronics, Karlsruhe Institute of Technology, Karlsruhe, Germany (e-mail: john.jelonnek@kit.edu).

to increase its efficiency [5], [6] and processing quality during the material processing, for instance, thermal curing of fiber composites and drying of porous foams. In the drying application, usually, the polymer foams have a non-uniform moisture distribution at the inlet. During processing, this situation can lead to temperature hot spots formation as the drying progresses due to non-uniform heating. Thus, wet spots surrounded by dry parts exist in the processed foam. And in case of over-drying, the foam may even take fire and damage the industrial system. Intelligent control of distributed microwave power sources is a possibility that might efficiently address the non-uniform moisture distribution [4] which requires non-invasive measurements of the unknown moisture distribution inside the foam. Thus, to estimate the moisture distribution in the foam, the MWT module is integrated with the high-power HEPHAISTOS system. In real-time monitoring, fast data acquisition (DAQ) from MWT is a critical task with less-computational resources and on-site integration. Using only one antenna with mechanical scanning for DAQ is not applicable. Hence, in our work a fixed array consisting of 7 X-band antennas is chosen for the MWT senor setup [7], [8]. The later section will provide a reason for the choice of the antenna and frequency band. Next, to obtain fast imaging results, a suitable MWT reconstruction algorithm is needed. Due to the limited angle setup, our present inverse problem is severely ill-posed [9], and thus applying quantitative reconstruction schemes are challenging.

Recently, a uniform diffraction tomography (UDT) algorithm was proposed in [10], [11] that correctly applies the stationary phase method to achieve improved estimates in comparison to diffraction tomography for embedded targets in a multilayered media. The reconstruction provided by the UDT is in real-time with monostatic antenna configuration and the algorithm incorporates only reflection data. For its suitable implementation in the fixed array case, the following guidelines should be taken into account: i) desired antenna type and specifications to achieve good spatial resolution, ii) to cover a large imaging domain, a high number of antennas or measurement points should be employed, and iii) the antennas should be positioned in close vicinity to meet the Nyquist sampling rate criteria. But, considering real-time monitoring in our industrial application, given guidelines are compromised. The use of large number of antennas increases the DAQ time and overall system cost. Thus, an obvious choice would be to use a fixed array, i.e. a multistatic MWT system with a low-number of antennas. However, with the

use of limited number of antennas, aliasing effect is seen in the reconstructed image and also spatial resolution is affected when multiple scatterers in the multilayered media are present. The former is caused due to the Nyquist criteria not being met. While, the latter are: first, less spectral components of scattered fields are present at the antennas aperture, second, in multiple scatterers case, the different spectral components from respective scatterers cannot be distinguished [12]–[14].

In this work, a multistatic uniform diffraction tomography algorithm (MUDT) for multilayered media is proposed [15]. The MUDT algorithm developed here specially caters for the measurement case of a multiple-input multiple-output fixed array sensor configuration. We first derive a systematic formulation for the MUDT by modeling our imaging domain as a multilayered media. Next, the concept of the effective aperture [16] is used for efficient implementation of the MUDT. To test the performance of the MUDT for 2-D reconstruction, a numerical study is conducted with 3-D scattering data for various moisture scenarios. Results are shown and compared with that of UDT. Non-ideal conditions like i) the top surface of the foam is random rough and ii) a case of random moisture distribution in the foam is also evaluated. Next, by knowing the location of targets, a fast optimization algorithm is derived by investigating the eigenvalues and eigenvectors of the scattering matrix to obtain the dielectric constant of the localized targets. In the final stage, the MUDT performance is tested with experimental data and compared with the UDT. Our work contributes in the following manner: i) it eliminates the need for time-consuming quantitative imaging for obtaining the dielectric constant of the target, ii) it enables the use of a low number of antennas that reduces the total cost of the system and provides good spatial resolution compared to the UDT, iii) there is no need to surround the media by antennas array i.e full-angle setup, iv) (to the best knowledge of the authors) it is first of its kind MWT applications in the industrial drying process. Ideas for this work are motivated by the initial work done by the authors which are represented in [17]–[21].

The paper is organized as follows: Section II provides an overview of the HEPHAISTOS system and MWT setup and details the MUDT qualitative method. Simulation results are shown to compare the MUDT and UDT imaging algorithm in Section III. Section IV describes how the dielectric constant of the targets is retrieved. Experimental results are investigated in Section V and finally Section VI shows the discussion and concluding remarks.

II. MICROWAVE TOMOGRAPHY SETUP

Unlike other MWT systems, the current MWT system is installed next to a high-power microwave drying system called HEPHAISTOS. It has a modular structure and consists of three microwave modules of the same type. Each module is $1\,\mathrm{m}$ long and equipped with six slotted waveguide antennas. The installed total output power of $36\,\mathrm{kW}$ in the $2.45\,\mathrm{GHz}$ ISM band allows continuous drying. In order to block the unwanted leakage of power from the HEPHAISTOS oven which can destroy the MWT system, a long X-band open waveguide antenna is chosen which also acts as a microwave high pass filter. Since the $2.45\,\mathrm{GHz}$ is in the cut-off region of the WR90 standard waveguide for the X-band, the electromagnetic (EM) fields decay with $e^{-\alpha z}$ where α is the attenuation constant, providing more than $100\,\mathrm{dB}$ isolation at $2.45\,\mathrm{GHz}$ along the waveguide antenna. An array of 7 waveguide antennas is located in semi-infinite free space, above the media. The 3-D configuration of the multistatic MWT, studied in this work is illustrated in Fig. 1 (left) with antenna array located on top of the foam.

The present imaging problem is cast as a multilayered media problem for a fixed cross-section (i.e. $y \times z$); the generalized geometry is shown in Fig. 1 (right). The distance of the antenna to the top of the polymer foam is t_0. In free space, the relative dielectric constant is denoted as $\epsilon_{r,0} = \epsilon_{r,N+1} = 1 - j0$ whereas the relative dielectric constant of the layer n is set to $\epsilon_{r,n}$. Next, we discuss the qualitative reconstruction approach in more detail. The formulation is represented in 2-D only, the
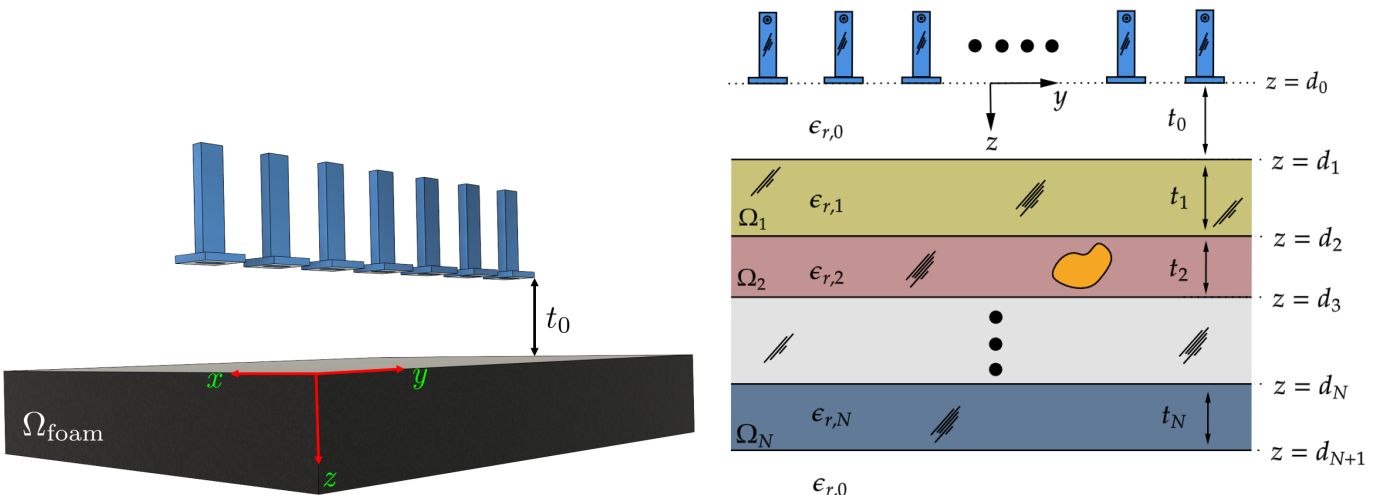
Fig. 1: Left: 3-D MWT setup used in this study to generate synthetic measurement data. Right: generalized geometry of our problem with N layers.

extension to a 3-D vector problem is straightforward but more cumbersome.

A. Forward Model

As shown in Fig.1 (right), the array of antennas is located in semi-infinite free space, above the media for illumination of medium. The variations of dielectric properties is considered in the z-direction only. Under the excitation by a point source, the electric field observed at the receiver positions, is given by the well-known Lippmann-Schwinger integral equation of the EM scattering problem and can be expressed in the following form [22], [23]

$$
\begin{aligned}
\vec{E}_{\text{tot}}^{(n)}(\vec{\rho}_r, \vec{\rho}_t) &= \vec{E}_{\text{inc}}(\vec{\rho}_r, \vec{\rho}_t) + \vec{E}_{\text{sct}}^{(n)}(\vec{\rho}_r, \vec{\rho}_t) \\
&= \vec{E}_{\text{inc}}(\vec{\rho}_r, \vec{\rho}_t) + k^2 \int_{\Omega_n} \bar{\bar{G}}_{\text{eb}}^{(n0)}(\vec{\rho}_r, \vec{\rho}') \cdot O(\vec{\rho}')\vec{E}_{\text{tot}}^{(n)}(\vec{\rho}')d\vec{\rho}',
\end{aligned}
\tag{1}
$$

where $\vec{E}_{\text{tot}}^{(n)}(\vec{\rho}_r, \vec{\rho}_t)$ represents the total electric field, $\vec{E}_{\text{inc}}(\vec{\rho}_r, \vec{\rho}_t)$ is the incident field and $\vec{E}_{\text{sct}}^{(n)}(\vec{\rho}_r, \vec{\rho}_t)$ denotes the received scattered field due to the unknown irregularities in layer n. $O(\vec{\rho}') = (\hat{\epsilon}(\vec{\rho}') - \epsilon_{r,n})$ is the object function. $\hat{\epsilon}(\vec{\rho}')$ is the profile of the dielectric constant of the target. $\Omega_n \subset \mathbb{R}^2$ is the region of interest which is the nth layer. Here, a time harmonic field is assumed. Hence, the complex time harmonic function $e^{-j\omega t}$ is eliminated from the equation. The term ω is the angular frequency. In (1), the vectors $\vec{\rho}_r = (y_r, z_r)$ and $\vec{\rho}_t = (y_t, z_t)$ represent observation and source points while $\bar{\bar{G}}_{\text{eb}}^{(n0)}(\vec{\rho}_r, \vec{\rho}_t)$ is the electric background (multilayered media without any scatterer inside) dyadic Green's function (DGF). The superscript $(n0)$ denotes that the source point is located in layer 0 and the observation point is in layer n.

By employing the first-order Born approximation, the total electric field $\vec{E}_{\text{tot}}^{(n)}$ can be replaced by the background electric field of the layer. Background electric field can be replaced by the Green's function due to the excitating the media by a point source. Moreover, utilizing the symmetry property of Green's function, the scattering electric field can be depicted as

$$
E_{\text{sct}}^{(n)}(\vec{\rho}_r, \vec{\rho}_t) = k^2 \int_{\Omega_n} G_{\text{eb}}^{(n0)}(\vec{\rho}_r, \vec{\rho}')O_n(\vec{\rho}')G_{\text{eb}}^{(n0)}(\vec{\rho}', \vec{\rho}_t)\, d\vec{\rho}'.
\tag{2}
$$

In the above expression, it is assumed that both transmitting and receiving antennas are x-polarized and equivalent current is predominantly x-polarized, so the term xx of the DGF is employed [24]. The spectral representation of the Green's function in layer n in transverse magnetic field to x (TM_x) case when the line source is located in region 0 is [25]

$$
\begin{aligned}
G_{\text{eb}}^{(n0)}(\vec{\rho}, \vec{\rho}_t) &= \frac{1}{\pi} \int_{-\infty}^{+\infty} \frac{1}{k_{z0}} \big[\tilde{T}_n^{\text{TM}}(k_y)e^{-jk_{zn}(z - z_t)} \\
&\quad \tilde{R}_n^{\text{TM}}(k_y)e^{+jk_{zn}(z - z_t)} \big] \cdot e^{-jk_y(y - y_t)}dk_y,
\end{aligned}
\tag{3}
$$

if $z > z_t$ and $Im(k_n^2 - k_y^2)^{\frac{1}{2}} < 0$ where k_y is the wavenumber in y-direction. $\tilde{T}_n^{\text{TM}}(k_y)$ and $\tilde{R}_n^{\text{TM}}(k_y)$ are the transmission and reflection coefficients in layer n respectively, and can be obtained by applying the boundary conditions between layers for the TM_x case. The asymptotic expression for

Green's function of the multilayered media is calculated using stationary phase approximation (SPA) and shown in Appendix A. The dispersion relation in the layer n is expressed by $k_{zn} = \sqrt{k_n^2 - k_y^2}$ and $k_n = k_0\sqrt{\epsilon_n}$ is the wavenumber in layer n while k_0 is the free-space wavenumber. As mentioned earlier, the electric field is composed of the incident and reflected parts, and since the contrast between the layers is small, the reflected electric field is not zero but negligible compared to the transmitted field inside that layer. To show this effect, consider a three layered medium with $\epsilon_{r,0} = 1$, $\epsilon_{r,1} = 1.16$, and $\epsilon_{r,2} = 1$ with thickness $t_0 = 10\,\text{cm}$, $t_1 = 8\,\text{cm}$, and t_2 is infinite free space, respectively. In the second layer, the real and imaginary parts of the total electric field at $8\,\text{GHz}$ and $12\,\text{GHz}$ are depicted in Fig. 2 (left) and Fig. 2 (right) respectively and compared with the finite element method (FEM) solution of COMSOL multiphysics. As a consequence, the Green's function of any layer is approximated only by the transmitted part as an asymptotic Green's function expression, i.e, $G_{\text{eb}}^{(n0)} \cong G_{\text{eb,T}}^{(n0)}$, and by substitution in (2), we obtained

$$
\begin{aligned}
E_{\text{sct}}^{(n)}(\vec{\rho}_r, \vec{\rho}_t) &= \frac{k^2}{\pi^2} \int_{\Omega_n} O_n(y', z') \Big(\int_{-\infty}^{+\infty} \int_{-\infty}^{+\infty} dk_y dk_y' \\
&\quad \frac{\tilde{T}_n^{\text{TM}}(k_y)\tilde{T}_n^{\text{TM}}(k_y')}{k_{z0}k_{z0}'} e^{-j\left[(k_y + k_y')y' - k_y y_r - k_y' y_t\right]} \\
&\quad \cdot e^{-j\left[(k_{zn} + k_{zn}')(z' - \sum_{q=0}^{n-1}t_q) + \sum_{q=0}^{n-1}(k_{zq} + k_{zq}')t_q\right]} \Big)d\rho',
\end{aligned}
\tag{4}
$$

where $G_{\text{eb,T}}^{(n0)}$ is replaced with the primed variable for the second integral. The above expression is the scattered field obtained due to the irregularities in layer n for a multistatic array scenario. It should be noted that while deriving this expression, it is assumed there are no irregularities in other layers. This representation enables us to use all the transmitter-receiver pairs of the multistatic configuration. In comparison to the monostatic configuration (with $y_r = y_t$), more spectral components of the embedded targets can be recorded by the multistatic array and also, higher order spectral frequency components are more discernible. For intuitive explanations of the above, consider two scatterers with centers y_1 and y_2 with the same z separated by distance L. The first phase term in (4) can be recast in the monostatic case as $(k_y + k_y')(y' - y_{ri})$ for the ith receiver. Since the spectral domain of integration is from negative infinity to infinity, a pair of high frequency terms (k_y, k_y') can satisfy $(k_{y1} + k_{y1}')(y_1 - y_{ri}) = (k_{y2} + k_{y2}')(y_2 - y_{ri})$. This implies the spectral components are indiscernible. As a consequence, secondary fields from the targets are indistinguishable at receiver position. So, a higher distortion effect is expected in multiple scatterers case in the monostatic case rather than a multistatic one.

B. Inversion scheme

To obtain the analytical expression of the object function given the scattered field information, we begin with the spatial Fourier transform (FT) of the received scattered field at y_r due to the transmitter at y_t. Next, by changing the variable
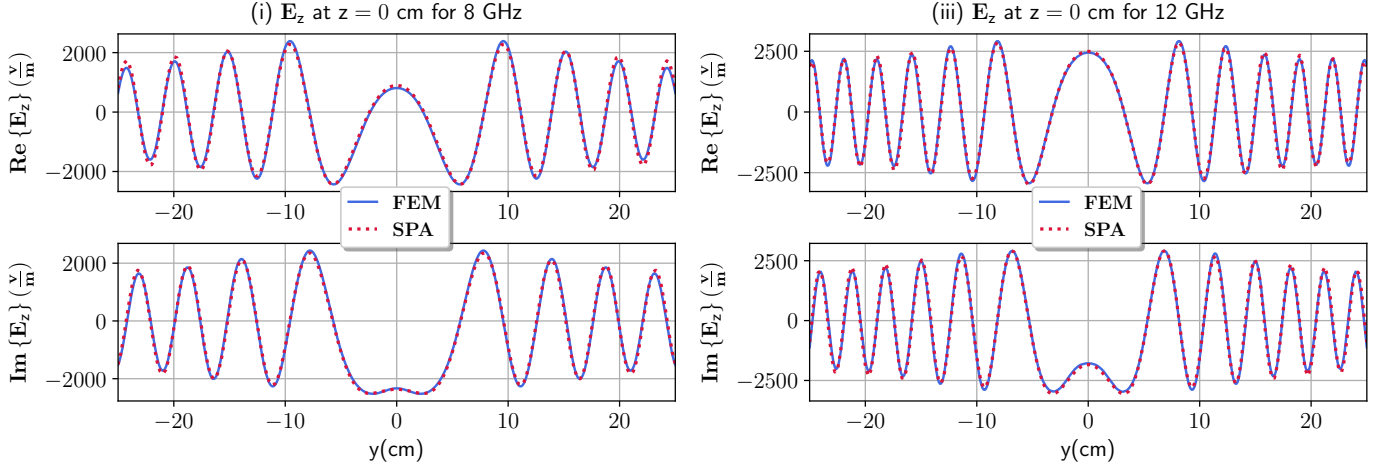
Fig. 2: The real (top) and imaginary (bottom) part of the total electric field inside a three layer media with dimension $50\,\text{cm} \times 8\,\text{cm}$ and $\epsilon_1 = 1.16$ for the dielectric layer at $8\,\text{GHz}$ (left) and $12\,\text{GHz}$ (right).

$k_y'' = k_y + k_y'$, the spectral representation of the scattered field in the multistatic case can be written using (4) as

$$
\tilde{E}_{\text{sct}}^{(n)}(k_y'', \omega) = \frac{2k^2}{\pi} \int_{\Omega_n} O_n(y', z') e^{-jk_y''y'} d\rho'
$$
$$
\left(\int_{-\infty}^{+\infty} dk_y \frac{k^2}{k_{z0}k_{z0}'} \tilde{T}_n^{\text{TM}}(k_y) \tilde{T}_n^{\text{TM}}(k_y'' - k_y) e^{-j[k_y(y_t - y_r)]} \right.
$$
$$
\left. {}^{-j\left[(k_{zn} + k_{zn}')(z' - \sum_{q=0}^{n-1} t_q) + \sum_{q=0}^{n-1}(k_{zq} + k_{zq}')t_q \right]} \right),
$$
$$
\cdot e \tag{5}
$$

where $k_{zn}' = \sqrt{k_n^2 - (k_y'' - k_y)^2}$. The term $k_y(y_t - y_r)$ in the phase of the inner integral is the difference between UDT and MUDT which is the consequence of considering the problem multistatic rather than monostatic. Using the SPA method, the second integral in (5) can be simplified, and above expression reduces to a simple form given

$$
\tilde{E}_{\text{sct}}^{(n)}(k_y'', \omega) = \frac{2}{\pi} \int_{\Omega_n} O_n(y', z') e^{-jk_y''y'} \frac{k^2}{\bar{k}_{z0}\bar{k}_{z0}'} \tilde{T}_n^{\text{TM}}(\bar{k}_y)
$$
$$
\tilde{T}_n^{\text{TM}}(k_y'' - \bar{k}_y) \left[\frac{2\pi}{k_0 z |\phi''(\bar{k}_y)|} \right]^{\frac{1}{2}} e^{-j\left(\frac{\beta}{2} + \frac{\pi}{4} \right)} e^{-j[\bar{k}_y(y_t - y_r)]}
$$
$$
{}^{-j\left[(\bar{k}_{zn} + \bar{k}_{zn}')(z' - \sum_{q=0}^{n-1} t_q) + \sum_{q=0}^{n-1}(\bar{k}_{zq} + \bar{k}_{zq}')t_q \right]}
$$
$$
\cdot e \qquad d\rho', \tag{6}
$$

where

$$
\phi''(\bar{k}_y) = -\frac{k_n^2}{k_0}\left(\frac{1}{\bar{k}_{zn}^3} + \frac{1}{\bar{k}_{zn}'^3} \right)\left(1 - \sum_{q=0}^{n-1} \frac{t_q}{z} \right)
$$
$$
- \sum_{l=0}^{n-1} \frac{k_q^2}{k_0}\left(\frac{1}{\bar{k}_{zq}^3} + \frac{1}{\bar{k}_{zq}'^3} \right), \tag{7}
$$

$$
\phi''(\bar{k}_y) = |\phi''(\bar{k}_y)| e^{j\beta}, \tag{8}
$$

and $\bar{k}_y$ is the solution of the following equation:

$$
\frac{1}{k_0 z}(y_t - y_r) +
$$
$$
\frac{1}{k_0}\left(-\frac{\bar{k}_y}{k_{zn}} + \frac{k_y'' - \bar{k}_y}{k_{zn}'} \right)\left(1 - \sum_{q=0}^{n-1} \frac{t_q}{z} \right) +
$$
$$
\sum_{q=0}^{n-1}\left(-\frac{\bar{k}_y}{k_{zq}} + \frac{k_y'' - \bar{k}_y}{k_{zq}'} \right)\frac{t_q}{k_0 z} = 0. \tag{9}
$$

Here, $\bar{k}_{zn}, \bar{k}_{zn}'$ are those defined earlier when k_y is replaced by $\bar{k}_y$. It should be noted the SPA is calculated with respect to the $k_0 z$ [10]. This assumption is in general case compared to applying the SPA with respect to the k_0 which provide a smooth transition at boundaries in the presence of a target.

Using the following spectral reflectivity function definition

$$
\tilde{O}_n(k_y'', k_z'', k)
$$
$$
= \int \int_{\Omega_n} \frac{O_n(y', z')}{\left[\frac{k_0 z}{2\pi} |\phi''(\bar{k}_y)| \right]^{\frac{1}{2}}} e^{-j(k_y''y + k_z''z)} dy dz, \tag{10}
$$

where $k_z'' = \bar{k}_z + \bar{k}_z'$, and substituting in (6), the object function can be obtained as represented in (11), where

$$
M(k_y'') = \frac{\omega\epsilon}{c^2}\left[\left(k_n^2 - (k_y'' - \bar{k}_y) \right)^{-\frac{1}{2}} + \left(k_n^2 - \bar{k}_y \right)^{-\frac{1}{2}} \right]. \tag{12}
$$

Equation (11) expresses a relation between the object function and the spatial Fourier transform of the received scattered field.

For implementation of the MUDT algorithm, the position of each transmitter-receiver pair in the multistatic array is approximated by its midpoint that is equivalent to a monostatic array configuration. This implies that each N_1 elements of multistatic array can be replaced by the $N_2 \geq N_1$ elements in the equivalent configuration and represented $N_1 : N_2$. In this case, the spatial sampling rate will be $L/(2N_1 N_2)$ where L is the length of N_1 elements in multistatic array. For example, $1 : 2$ denotes 1 elements of the multistatic array is replaced

$$O_n(y,z) = \frac{\int_\omega \int_{-\infty}^{+\infty} \frac{k_{z0}k_{z0}''}{k_n^2} \frac{e^{j\left(\frac{\beta}{2} + \frac{\pi}{4}\right)}}{\tilde{T}_n^{\mathrm{TM}}(\bar{k}_y)\tilde{T}_n^{\mathrm{TM}}(k_y'' - \bar{k}_y)} e^{j\left[\bar{k}_y(y_t - y_r)\right]} e^{j\left[k_{zn}'' \sum_{q=0}^{n-1} t_q - \sum_{q=0}^{n-1} k_{zq}'' t_q\right]} \tilde{E}^{\mathrm{sct}}(k_y'', k) M(k_y'') dk_y'' d\omega}{\sqrt{\frac{\pi}{8}} \int_\omega \int_{-\infty}^{+\infty} \frac{M(k_y'')}{\left[k_0 z |\phi''(\bar{k}_y)|\right]^{\frac{1}{2}}} dk_y'' d\omega}$$

(11)

TABLE I: Dielectric constant of the foam with different moisture contents $\mathrm{M}_w\%$ on wet-basis.

$\mathrm{M}_w\%$	0	30	36
ϵ_r	$1.16\text{-}j0.01$	$1.69\text{-}j0.1$	$1.87\text{-}j0.12$

by 2 element in the equivalent monostatic array this implies that 13 sampling points exist for 7 element antenna array. Conceivably, the aforementioned procedure is stated to be very similar to effective aperture concept utilized in multistatic mm-wave imaging system [26]–[28].

III. NUMERICAL STUDIES

In this section, the proposed MUDT algorithm is numerically tested for different moisture scenarios, and their results are compared with UDT. To generate the numerical data from the MWT setup shown in Fig. 1 (Left), the 3-D time-domain solver of the commercial software CST Studio Suite is used. The data are generated in X-band range with a frequency step of $5\,\mathrm{MHz}$ and stored in terms of a scattering matrix of size 7×7. Moisture distribution is modeled as wet-spots in a spherical shape with the defined dielectric constant corresponding to the different moisture levels. The mapping between the dielectric constant and the wet-basis moisture levels, measured by cavity-perturbation method as well as transmission line technique at $2.45\,\mathrm{GHz}$ is given in Table I [29]. For this characterization, the polymer foam density is $23\,\frac{\mathrm{kg}}{\mathrm{m}^3}$. To obtain the qualitative image using the MUDT, in addition to the diagonal element of the scattering matrix, the $S_{i(i+1)}, (i = 1, 2, \ldots, 6)$ are used as well for the image reconstruction. This implies a $1 : 2$ equivalent monostatic array as described in the previous section. Also, an antennas de-embedding is performed to convert the received scattered fields to the electric fields [30], [31]. Moreover, it might be applicable to mention since the contrast between the foam and its below layer is assumed to be small, our problem is equivalent to the half-space problem. Some corresponding equations related to the half-space case are shown in Appendix B.

Three different scenarios are considered to show the performance of the proposed MUDT in comparison to the UDT imaging algorithm. In the first scenario, only one wet-spot with radius $1\,\mathrm{cm}$ and moisture level of 42% ($\epsilon = 2$) is considered in the polymer foam. The reconstruction from the UDT and MUDT are depicted in Fig. 3 with the red lines represent the true location of the wet-spot inside the foam. Note that
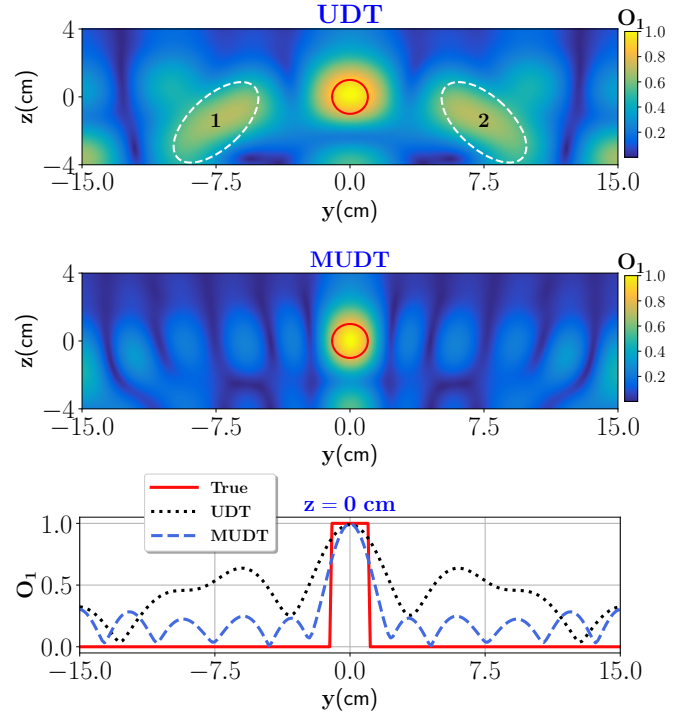
Fig. 3: Reconstruction of one wet-spot moisture case with UDT (top) and MUDT (middle) where the true location is marked by red circle. The bottom figure shows the comparison of UDT and MUDT with the true case for the object function values located at $-15\,\mathrm{cm} \leq \mathrm{y} \leq 15\,\mathrm{cm}$ for $\mathrm{z} = 0\,\mathrm{cm}$.

the normalized value of the object function is plotted. It is clear that the MUDT outperforms UDT in identifying the target. Also, strong aliasing effect are observed in UDT as marked by regions 1 and 2. In contrast, the aliasing effect is resolved in the MUDT since the Nyquist sampling rate criteria is satisfactorily met in the multistatic configuration. Further, the object function at $z = 0\,\mathrm{cm}$ for UDT and MUDT are plotted in Fig. 3 (bottom) and reconstruction differences can be better observed.

In the second scenario, two wet-spots with a moisture levels of 42% ($\epsilon = 2$) and 26% ($\epsilon = 1.5$), respectively. The radius of the wet-spots are kept the same as the previous case and they are located at $10\,\mathrm{cm}$ distance apart. This case is considered here since the HEPHAISTOS oven works at $2.45\,\mathrm{GHz}$, hence the heating pattern of drying is in the range of $\frac{\lambda_{\mathrm{oven}}}{2} \approx 6\,\mathrm{cm}$. Therefore it is imperative to estimate the wet-spot locations
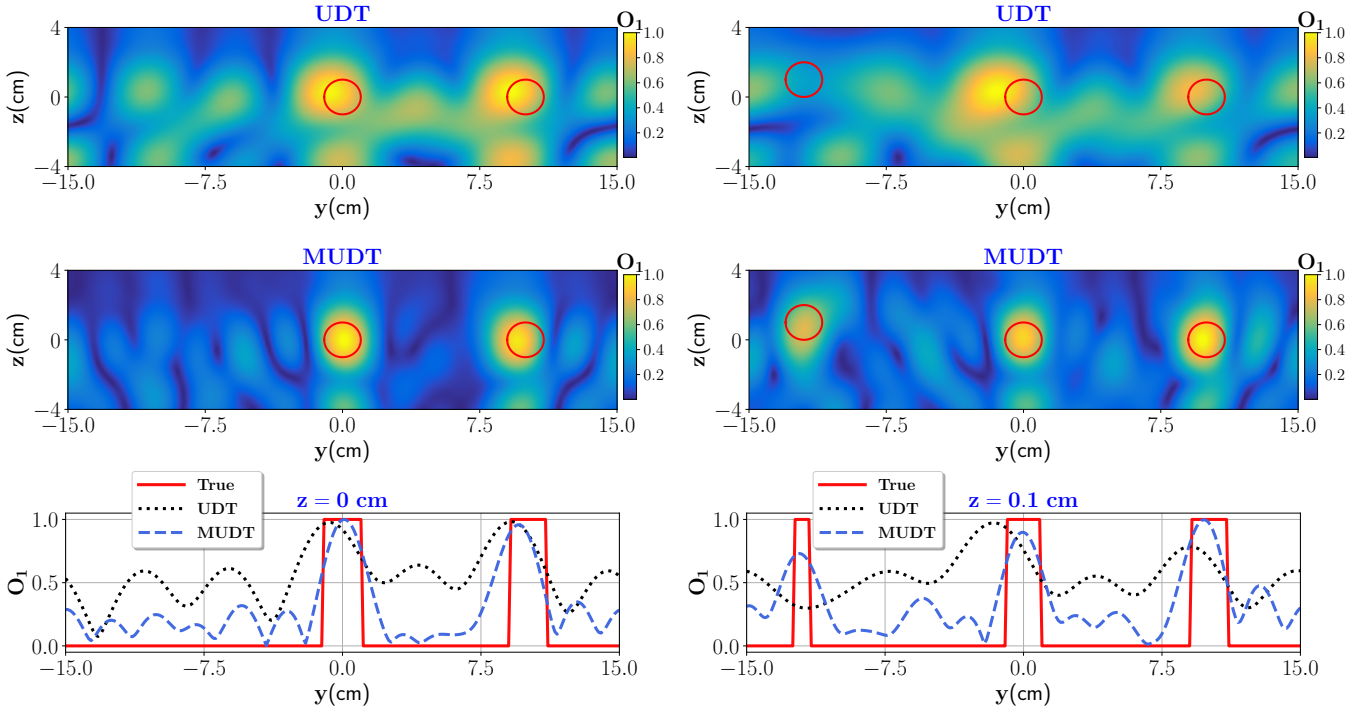
Fig. 4: Reconstruction of two wet-spots (left) and three wet-spots (right) moisture case with UDT (top) and MUDT (middle). The bottom figure shows the comparison of UDT and MUDT with the true case for the object function values located at $-15\,\text{cm} \leq y \leq 15\,\text{cm}$ for (left) $z = 0\,\text{cm}$, and (right) $z = 0.1\,\text{cm}$.

with a similar spatial resolution to control the power efficiently. In other words, the power of the magnetrons is adjusted based on the moisture distribution inside the polymer foam. The reconstructed image using the UDT and MUDT is shown in Fig. 4 (left column) where the bottom figure represents the compared object function at $z = 0\,\text{cm}$ with respect to the true case. Interestingly, in UDT, in addition to the aliasing effect, a distortion in the reconstructed image is observed. It implies that the scattered fields from the targets are indistinguishable at the receiver position. This effect will be more prominent by increasing the number of targets in the medium. However, in the MUDT, these scattered fields can be recorded by more receivers, resulting in discernible wet-spots.

In order to investigate the robustness of the MUDT imaging algorithm under the multiple scatterers case, in the third scenario, three wet-spots with same moisture levels of 42% and radius of $1\,\text{cm}$ are considered. The three wet-spots are located at $(-12\,\text{cm}, 1\,\text{cm})$, $(0\,\text{cm}, 0\,\text{cm})$, and $(10\,\text{cm}, 0\,\text{cm})$, respectively in the $y - z$ plane. As can be seen from Fig. 4 (right column), UDT at first fails to reconstruct all the targets in the imaging domain, see the left circle (which indicates true position of the target). More so, the reconstructed middle and the right wet-spots are shifted and distorted. As explained earlier, these effects are due to interference of the spectral components at receiver positions. In comparison, reconstruction with MUDT is appropriate for all wet-spots especially the left target. Also the shift and distortion of targets are negligible. However some minor aliasing effect are present which can be eliminated by taking into account more elements of the scattering matrix. Further, to evaluate the closeness

of the reconstructions, cuts along the y-axis of Fig. 4 (right column) are plotted. As can be observed, using the MUDT, the estimated position and shape of the targets are close to the true case and the resolution is improved.

In the next part, we investigate the performance of the proposed technique when i) the surface of the polymer foam is random rough and ii) when the wet-spots are surrounded by inhomogeneities. These scenarios are undertaken considering pre-preparation drying process defects.

A. Random rough surface

In practical scenarios, it has been observed that the polymer foam can also have some uncertainty on the surface i.e., when the surface has roughness. To investigate the performance of the MUDT in this case, we consider a polymer foam with a top surface being randomly rough surface (RRS) and modeled [32] as

$$z(y) = \sum_{m=-M}^{M} m^{-\beta} G_m \cos\left(2\pi m y + U_m\right). \quad (13)$$

Here, m is the integer number representing the spatial frequency and β denotes the spectral exponent, G_m is realized as $G_m \sim \mathcal{N}(\mu, \sigma)$ with mean μ and standard deviation σ, and $U_m \sim \mathcal{U}(0, 2\pi)$. The term $\mathcal{N}, \mathcal{U}$ denotes Gaussian and uniform distribution, respectively.

In Fig. 5, compared are the real and imaginary parts of the electric field asymptotic formulation [24] and FEM for a dry foam with two different degrees of roughness at $8\,\text{GHz}$. Here, the asymptotic fields of the three-layer media with the rough
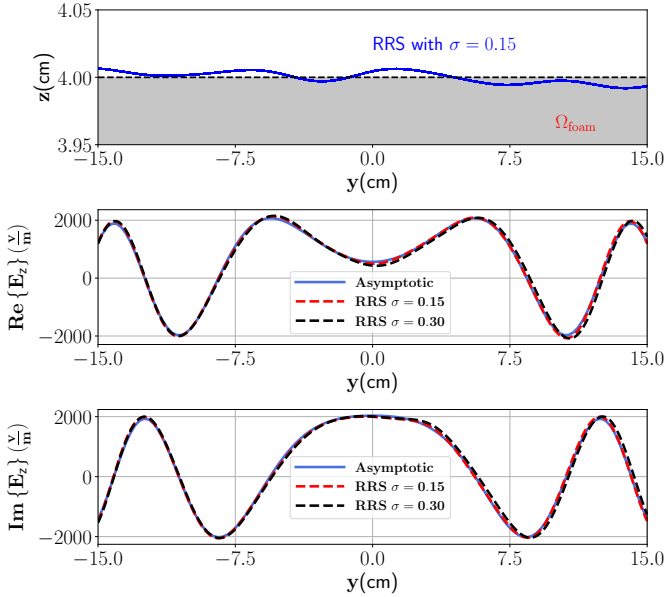
Fig. 5: Top figure shows the foam with modelled roughness and its mean height. Electric fields real (middle) and imaginary (bottom) parts derived using analytical formulation are compared with the FEM results of a rough surface with an $\sigma = 0.15$ and $\sigma = 0.3$ are probed at $z = -14\,\text{cm}$ and $-15\,\text{cm} \leq y \leq 15\,\text{cm}$. For this study, the line source was located at $z = 0\,\text{cm}$.

surface for the first interface is estimated using the SPA under the $\sigma = 0$ and $\beta = 0$. We observe that under the moderate random rough surface, the scattered fields received by antennas slightly change compared to the normal scenarios when RMS height = 0. So, the average distance from each antenna to the top surface of the foam is considered, i.e., $h = \langle h_i \rangle$, $i = 1, 2, \cdots N$, where $\langle \cdot \rangle$ is the mean operator.

To evaluate the performance of the MUDT, a wet-spot with 30% moisture $(1.69 - j0.1)$ with radius $1\,\text{cm}$ at position $(0\,\text{cm}, 0\,\text{cm})$ is considered inside the foam with dielectric constant $1.16 - j0.01$ and a moderate rough surface with the following parameters: $\mu = 0$, $\sigma = 0.15$, and $\beta = 0.8$. Reconstructed image using the MUDT algorithm is depicted in Fig. 6. It can be depicted from the figure that though the location of the wet-spot is correctly estimated but compared to the polymer foam with the smooth surface, the shadow images are more prominent. This is due to the multiple scattering between the bottom layer of the foam and the rough surface that is not taken into account by Green's function. Furthermore, with increasing the roughness of the top interface, the validity of the current asymptotic expression holds weak since electromagnetic fields inside the layer can not be fully estimated. It can lead to more strong artifacts in the reconstruction.

B. Random Media

Consider a polymer foam where the dielectric constant distribution of the medium is not constant and has random values. In other words, wet-spots are surrounded by inhomogeneities
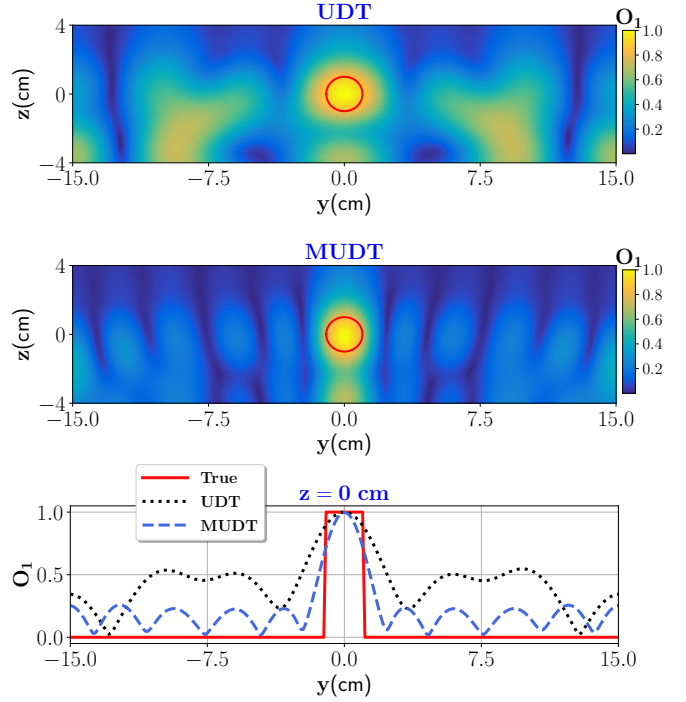
Fig. 6: Reconstruction of one wet-spot moisture case with UDT (top) and MUDT (middle) for the random rough surface with $\mu = 0$, $\sigma = 0.15$, and $\beta = 0.8$. The bottom figure shows the comparison of UDT and MUDT with the true case for the object function values located at $-15\,\text{cm} \leq y \leq 15\,\text{cm}$ for $z = 0\,\text{cm}$.

and, the dielectric constant of the layer can be expressed as $\epsilon(\vec{r}) = \epsilon_n + \epsilon_f(\vec{r})$ where ϵ_f is the randomly fluctuating part of the dielectric constant and ϵ_n denotes the mean dielectric constant such that the ensemble average $\langle \epsilon(\vec{r}) \rangle = \epsilon_n$, and $\vec{r} = y\hat{y} + z\hat{z}$ is the spatial position. Here, we assume the average dielectric constant of the polymer foam is known. The fluctuating inhomogeneities have a zero-mean Gaussian random variable with a Gaussian correlation function [33], [34]

$$C(\vec{r}_1, \vec{r}_2) = \exp\left(-\frac{||y_1 - y_2||^2}{l_y^2} - \frac{||z_1 - z_2||^2}{l_z^2} \right), \quad (14)$$

where l_y and l_z are the characteristic length components. In this case, the deterministic form of the Green's function is not known. However, for the tenuous random media, the Green's function can be expressed as follows [35]

$$\langle \bar{\bar{G}}(\vec{r}, \vec{r}_t) \rangle = \bar{\bar{G}}^{(0)}(\vec{r}, \vec{r}_t) + \Delta^2 \langle \bar{\bar{G}}^{(2)}(\vec{r}, \vec{r}_t) \rangle \\ + \Delta^4 \langle \bar{\bar{G}}^{(4)}(\vec{r}, \vec{r}_t) \rangle + \cdots, \quad (15)$$

where $\Delta = \mu\omega^2 \sqrt{\langle \epsilon_f(\vec{r}) \rangle^2}$. Under the assumption where there is weak correlation between the unknown inhomogeneities i.e., $C(\vec{r}_1, \vec{r}_2) \approx 0$ (the multiple reflections between the fluctuating parts is ignored), the Green's function can be approximated by only the first term, i.e., $\langle \bar{\bar{G}}(\vec{r}, \vec{r}_t) \rangle \approx \bar{\bar{G}}^{(0)}(\vec{r}, \vec{r}_t)$. A random media with the Gaussian distribution with characteristic length $l_x = 5\,\text{cm}$, $l_y = 2\,\text{cm}$, and $l_z = 3\,\text{cm}$ is modeled in the
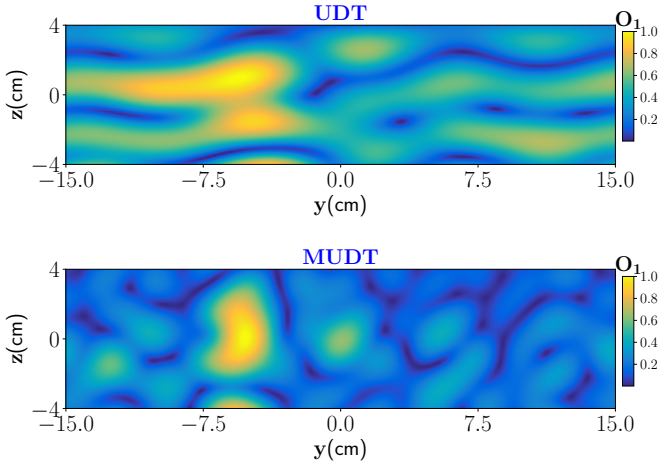
Fig. 7: Reconstruction of random media containing one dominant wet-spot with UDT (top) and MUDT (bottom).

CST Studio Suite using 3-D form of (14). In our random media model, only one dominant and well resolved wet-spot is present in the $y - z$ plane of the antennas and rest of the plane has weak fluctuations. The reconstructed images from the UDT and MUDT is shown in Fig. 7. As can be seen, the dominant and well resolved wet-spot is accurately detected by the MUDT.

IV. MOISTURE LEVEL ESTIMATION

In this part, we obtain the dielectric constant of the reconstructed targets from MUDT using the singular value decomposition (SVD) and minimization approach [20]. Starting with (2) and expressing it in the following matrix form for each frequency point

$$E_{\text{sct}} = [\mathcal{L}_{\text{o}}] \left[(\hat{\epsilon} - \epsilon_{r,n}) \right], \tag{16}$$

where E_{sct} is of size $N \times 1$, $\mathcal{L}_o$ is the linear operator with size $N \times M$, and $(\hat{\epsilon} - \epsilon_{r,n})$ is the object function of size $M \times 1$. The term N denotes the total number of transmitter and receiver pairs and term M denotes total number of pixels in the imaging domain. The linear operator $\mathcal{L}_{\text{o}}$ is given as

$$\mathcal{L}_{\text{o}} = k^2 \int_{\Omega_n} g_{T,r}^{(n0)}(\vec{\rho}') g_{T,t}^{(n0)\top}(\vec{\rho}') \, d\vec{\rho}'. \tag{17}$$

The term $g_{T,r}(\vec{\rho}')$ and $g_{T,t}(\vec{\rho}')$ are the steering vectors of the transmission part of the background green's function, expressed by

$$g_T^{(n0)} = \left[G_{\text{eb,T}}^{(n0)}(\vec{\rho}, \vec{\rho}_1), G_{\text{eb,T}}^{(n0)}(\vec{\rho}, \vec{\rho}_2), \cdots, G_{\text{eb,T}}^{(n0)}(\vec{\rho}, \vec{\rho}_N) \right]^{\top}, \tag{18}$$

where $(\cdot)^{\top}$ stands for the transpose operator.

To calculate the dielectric constant, information from MUDT with thresholding operation and support domain of the targets is used before the next step. The thresholding operation on MUDT is performed to separate the dry part domain and wet-spot domain. The choice of the thresholding value is heuristic and is done to separate the dry part from

the wet-spots. The thresholding operation, $\wp$, on the object function in (11) is performed as

$$O_n = \begin{cases} \epsilon_{r,n} \ \forall \ O_n(y, z) \mid_{\wp < 0.5} & \in \Omega_{\text{d}} \\ \epsilon_g \ \forall \ O_n(y, z) \mid_{\wp > 0.5} & \in \Omega_{\text{h}}. \end{cases} \tag{19}$$

The domain Ω_{h} will be assigned to the background dielectric constant ($\epsilon_{r,n}$) and the rest domain will be assigned to the unknown dielectric constant (ϵ_g). Using SVD, the scattering matrix can be decomposed into the eigenvectors and eigenvalue matrices, i.e, $\text{SVD}(E_{\text{sct}}^{(n)}) = U \Sigma V^{\top}$ where U is an complex unitary matrix, Σ is an rectangular diagonal matrix with non-negative real numbers on the diagonal, and V is an complex unitary matrix. The column of U and V form a set of orthogonal vectors or eigenvectors and Σ consists of eigenvalues. The number of non-zero eigenvalues represents the number of target in the media and, the pth target associates with p^{th} eigenvalue of the matrix Σ [21], [36]. Hence, in order to obtain the dielectric constant of the pth target in the media, associated eigenvalue from the theory and measurement will be compared for the different guess dielectric constant values with the following minimization function

$$\widehat{\epsilon} = \arg \min_{\epsilon_g} \sum_f \left\| \frac{\sigma_p^{\text{Meas}}}{\sigma_p^{\text{Meas}} \Big|_{\epsilon_c}} - \frac{\sigma_p^{\text{Th}} \Big|_{\epsilon_g}}{\sigma_p^{\text{Th}} \Big|_{\epsilon_c}} \right\|^2, \tag{20}$$

where $\sigma_p^{\text{Th}} \Big|_{\epsilon_g}$ denote the pth eigenvalue of a obtained theoretically where modified domain in (19) is used to calculate the (20). The term $\sigma_p^{\text{Th}} \Big|_{\epsilon_c}$ denotes the pth eigenvalue when the calibration target with given relative dielectric constant (ϵ_c) is used in the media. On the other hand, σ_p^{Meas} is the pth eigenvalue of the measurement and, $\sigma_p^{\text{Meas}} \Big|_{\epsilon_c}$ is the pth eigenvalue of the measured data once the calibration target is embedded into the media. In the latter case, the relative dielectric constant is ϵ_c. It should be noted, $\hat{\epsilon}$ becomes minimum when the guess value of dielectric constant is close to the true value. A Poly(methyl methacrylate) (PMMA) target with the dielectric constant $\epsilon_c = 3.2$ is chosen for the calibration in (20).

As an first example, we evaluate the case where one wet-spot is located inside a polymer foam. The location of the wet-spot was previously obtained using the MUDT in Fig. 3. After thresholding operation, the dry and the moisture parts are separated and assigned to dielectric values of $\epsilon_{r,1}$ and unknown ϵ_g, respectively. Since only one target is visible in the reconstruction, it is evident that only one dominant singular values will exist in the measured scattering matrix. To solve for the minimisation problem in (20), the guess values are chosen based on the dielectric characterization of the foam depicted in Table I. The MUDT reconstruction with thresholding operation, and estimated dielectric value of the moisture wet-spot are shown in Fig. 8 (top left and middle left). The closeness of the estimate to the true value, $\epsilon = 2$, is shown in the 1-D plot of the Fig. 8 (bottom left).

In the next scenario, two wet-spots with the different moisture level inside the polymer foam are investigated. The
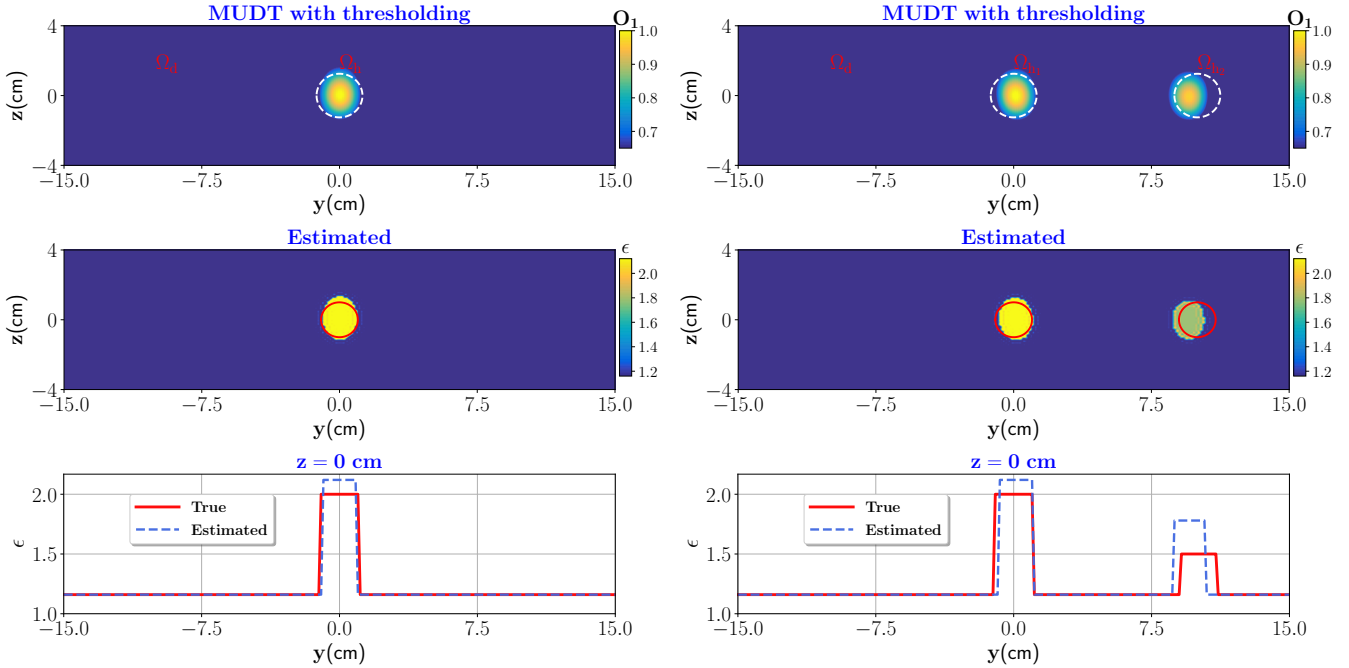
Fig. 8: MUDT reconstruction for (top left) one wet-spot and, (top right) two wet-spots with thresholding. Their corresponding estimated dielectric constant values are shown in middle left and right, respectively. The 1-D plots at the bottom show the comparison of the estimated values with the respective true cases.

TABLE II: Results of error analysis for different diameters.

d (cm)	2	3	4	5	6
ϵ	2.07	2.39	2.45	2.51	2.78
RMSE (%)	3.38	16.32	18.37	20.32	28.06

TABLE III: Results of error analysis for different SNR.

SNR (in dB)	zero noise	30	20	15	12
ϵ	2.07	2.22	2.41	2.46	2.95
RMSE (%)	3.38	9.91	17.01	18.69	32.2

domain of the wet-spots Ω_{h_1}, Ω_{h_2} was previously obtained using the MUDT in Fig. 3. As mentioned earlier, the locations of wet-spots are visible and, after applying the thresholding, the foam domain is separated into the dry part and two wet-spots. In this case, there exist two dominant eigenvalues which correspond to two wet-spots domain. Since the center wet-spot is dominant out of two, the largest eigenvalue is assigned to it and, the second largest eigenvalue is for the second wet-spot. The minimization problem is solved separately and in parallel to obtain the dielectric constant of the wet-spots. The MUDT reconstruction with thresholding operation, and estimated dielectric value of the moisture wet-spot are shown in Fig. 8 (top right and middle right). The closeness of the estimate to the true value of the wet-spots, $\epsilon_1 = 2$ and $\epsilon_2 = 1.5$, is shown in the 1-D plot of the Fig. 8 (bottom right).

It is worth noting by increasing the diameter (d) of the moisture size, the estimation error of the dielectric constant will increase. It is because the proposed method is based on the Born approximation. So, the conditions for replacing the total field with the incident one inside the irregularities cannot sufficiently be met by increasing the diameter. For illustrating this outcome, the estimated dielectric constant and its RMSE error for one wet-spot region are shown in Table II. In addition, the estimation error will also increase with increasing the

signal-to-noise ratio (SNR) as shown in Table III for a fixed diameter of one wet-spot case.

V. EXPERIMENTAL RESULTS

As shown in Fig. 9, an MWT setup is integrated with a high-power microwave drying system. It consists of 11 WR90 open-ended waveguide antennas (VSWR 1.03 : 1). A 2 × 16 USB 9164C Keysight Solid state switch matrix is used to connect (with the phase stable cables with phase stability 3° at the maximum frequency) the antennas to the Agilent N5224A vector network analyzer (VNA). It should be mentioned to remove the unwanted reflections, a waveguide calibration is fulfilled. Communication between the controlling computer, switch, and VNA is performed through the Ethernet cable. Processing of DAQ is completely automated using MATLAB R2018b. Antennas are located in semi-infinite free-space from $-27.5\,\text{cm}$ to $27.5\,\text{cm}$ along the y-axis and the distance of the antenna to the polymer foam is $12\,\text{cm}$, and the center to center distance between two adjacent antennas is $5\,\text{cm}$.

In the first experiment, two PTFE Teflon spheres with a radius of $1.2\,\text{cm}$ and dielectric constant $\epsilon_{\text{tef}} = 2.1$ are used as the test targets. They are placed inside the foam with their centers located at $(0\,\text{cm}, -2\,\text{cm}, 0\,\text{cm})$ and, $(0\,\text{cm}, -8\,\text{cm}, 0\,\text{cm})$. A background subtraction is applied to extract the scattering field due to scatterer inside the polymer foam. Reconstructed
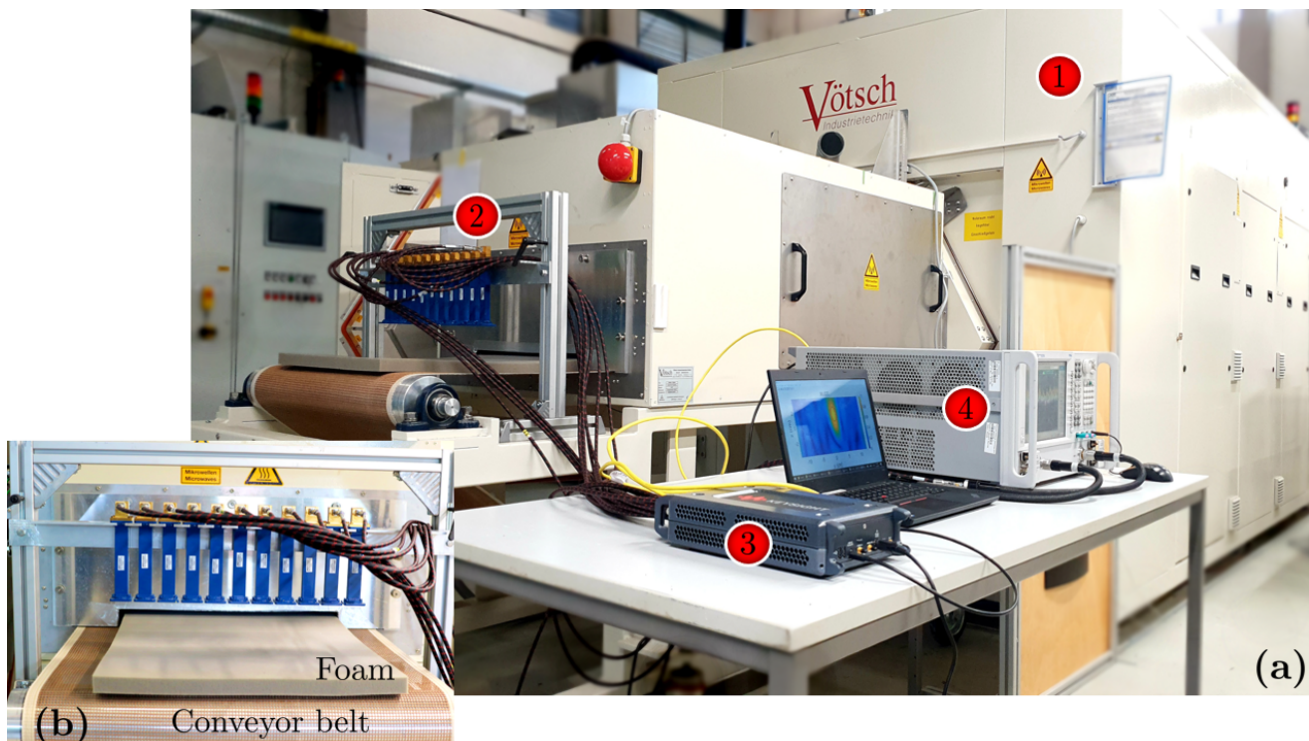
Fig. 9: (a) MWT system and its integration with the HEPHAISTOS (number Tag 1) is shown. The number Tags 2, 3, and 4 shows the MWT system, Solid state switch, and VNA respectively. (b) shows the enlarged view of the MWT sensor array of X-band open-ended waveguide antennas. Note here only 7 antennas are used in the measurement with the polymer foam of thickness $7.6\,\text{cm}$.

based on UDT is depicted in Fig. 10 (a). The expected aliasing effect and a heavy distortion are observed, and UDT fails to reconstruct targets in the imaging domain. However, MUDT correctly reconstructs all positions and provides a negligible shadow image in Fig. 10 (b). Further, to evaluate the closeness of the reconstructions, cuts along the y-axis of Fig. 10 (c) are plotted. As can be observed, using the MUDT, the estimated position and shape of the targets are close to the true case, and different targets are resolved. We follow similar steps described in Section IV to obtain the dielectric constant of the targets. The estimated dielectric constant of the targets are shown in Fig. 10 (d). The closeness of the estimate to the true value, $\epsilon = 2.1$, is shown in the 1-D plot of the Fig. 10 (e).

In the second experiment, a moisture wet-spot is inserted in the polymer foam. To create the wet-spot moisture target, a spherical foam of diameter 2.5 ± 0.1 cm and with 36% wet-basis moisture level ($\epsilon \approx 1.87 - j0.12$) is chosen. An approximate location of the target inside the foam is centered at $(0\,\text{cm}, -3.5\,\text{cm}, 1.2\,\text{cm})$. Reconstruction image based on UDT is depicted in Fig. 11 (a). As supported by the simulation, in this case, the location of the wet-spot is reconstructed, but, a strong aliasing effect is observed. However, with the MUDT, in addition to eliminating the aliasing effect, the spatial resolution is also increased as shown in Fig. 11 (b). For better comparison in the reconstruction, cuts along the y-axis of Fig. 11 (c) are plotted. The estimated dielectric constant value of wet-spot obtained using the SVD approach and its comparison to the true case are shown in Fig. 11 (d) and (e), respectively.

VI. CONCLUSION

In this paper, a novel 2-D MUDT imaging algorithm has been presented for a fixed-array based MWT setup to image moisture distribution in a polymer foam undergoing industrial drying process. Its computationally efficient formulation is derived by assuming the imaging domain as planar multilayered media and using first-order Born approximation with proper DGF expression and SPA solution. The proposed algorithm is an extended version of the UDT algorithm and formulated to support multiple-input multiple-output antennas data. In the former method, raster scanning or single-input single-output data should be available that is time consuming and not fit for our current industrial application of the MWT.

Numerical examples with 3-D multistatic scattering data for the considered sparse moisture scenarios in the foam has demonstrated that MUDT provides significant improvement over UDT in reconstructing aliasing-free and distortion-less images, and in resolving multiple-scatterers in the multilayered media. Also, the proposed approach offers efficient performance in locating scatterer(s) domain for special cases like when top surface of the foam is assumed random rough and for the case when the imaging domain is a random inhomogeneous media. Unique to this approach, a method is also presented to estimate the electrical properties of the scatterer which corresponds to moisture level. Here, the dielectric constant of the detected moisture is obtained by taking the SVD from the scattering matrix and by comparing the pth eigenvalue of the pth scatterer from the theory and the experiment. The proposed
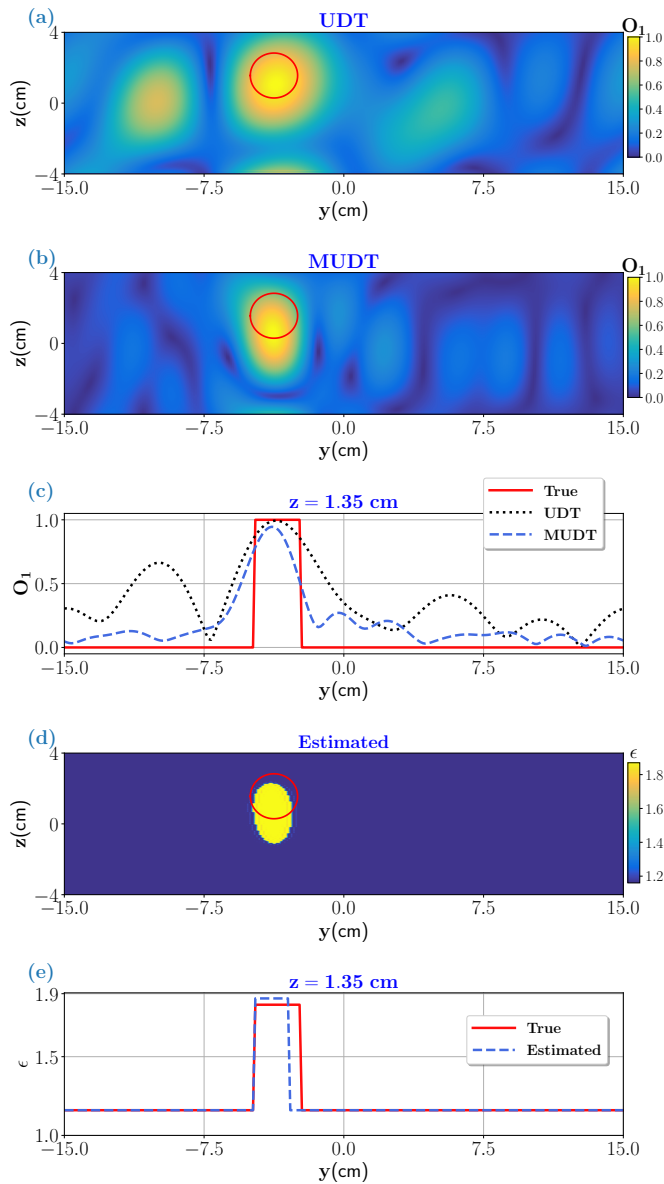
Fig. 10: Reconstruction of two Teflon targets embedded in the foam is shown in (a) with UDT approach, (b) with MUDT approach, and (c) show a the comparison of the UDT and MUDT approach with the true case for the object function values located at $-15\,\text{cm} \leq \text{y} \leq 15\,\text{cm}$ for $\text{z} = 0\,\text{cm}$. The estimated dielectric values of the reconstructed targets using SVD approach is shown in (d) and its comparison against the true case at $z = 0\,\text{cm}$ as a 1-D plot is depicted in (e).

Fig. 11: Reconstruction of moisture wet-spot in the foam is shown in (a) with UDT approach, (b) with MUDT approach, and (c) show a the comparison of the UDT and MUDT approach with the true case for the object function values located at $-15\,\text{cm} \leq \text{y} \leq 15\,\text{cm}$ for $\text{z} = 1.35\,\text{cm}$. The estimated dielectric values of the reconstructed targets using SVD approach is shown in (d) and its comparison against the true case at $z = 1.35\,\text{cm}$ as a 1-D plot is depicted in (e).

MUDT imaging algorithm is verified with the experimental data from our designed MWT setup.

It could be concluded the proposed MUDT imaging algorithm i) is compatible with low number of antennas to achieve fast data collection and hence reduce overall cost of the system, and ii) provides good spatial resolution, iii) eliminates the need for quantitative imaging algorithm (due to ill-posedness of the problem). The aforementioned points make the proposed combined imaging algorithm suitable for microwave drying industrial process. Future work involves

integrating the MWT with feed-forward unit of the control system of the industrial drying system and in supporting the visualization analysis using augmented reality [37]. Though the algorithm performance was tested for our industrial application, but the framework is applicable for general inverse scattering problems, like ground penetrating radar, through wall imaging, medical applications etc.

APPENDIX A
APPROXIMATE GREEN'S FUNCTION OF MULTILAYERED MEDIA

For obtaining a closed-form of the Green's function of the multilayered media, first we put a line source in layer 0. In this case, the transmission and reflection coefficients of the Green's function in layer n in TM_x case can be expressed in matrix form as

$$\begin{bmatrix} \tilde{R}_{n+1}^{\text{TM}} e^{+jk_{z(n+1)}d_{(n+1)}} \\ \tilde{T}_{n+1}^{\text{TM}} e^{-jk_{z(n+1)}d_{(n+1)}} \end{bmatrix} = \bar{\bar{V}}_{n(n+1)}^{\text{TM}} \begin{bmatrix} \tilde{R}_{n}^{\text{TM}} e^{+jk_{zn}d_{n}} \\ \tilde{T}_{n}^{\text{TM}} e^{-jk_{zn}d_{n}} \end{bmatrix}, \tag{A1}$$

where

$$\bar{\bar{V}}_{n(n+1)}^{\text{TM}} = \frac{1}{2}(1 + \frac{k_{zn}}{k_{z(n+1)}}) \times$$
$$\begin{bmatrix} e^{+jk_{z(n+1)}t_n} & -\tilde{R}_{n(n+1)}^{\text{TM}} e^{+jk_{z(n+1)}t_n} \\ -\tilde{R}_{n(n+1)}^{\text{TM}} e^{-jk_{z(n+1)}t_n} & e^{-jk_{z(n+1)}t_n} \end{bmatrix}, \tag{A2}$$

$\tilde{R}_{n(n+1)}^{\text{TM}}$ is the Fresnel reflection coefficients between layers n and $n+1$ which is written as

$$\tilde{R}_{n(n+1)}^{\text{TM}} = \frac{k_{zn} - k_{z(n+1)}}{k_{zn} + k_{z(n+1)}}, \tag{A3}$$

and, $\tilde{T}_{n(n+1)}^{\text{TM}}$ is the Fresnel transmission coefficient for the layers n and $n+1$ which is written as

$$\tilde{T}_{n(n+1)}^{\text{TM}} = \frac{2k_{zn}}{k_{zn} + k_{z(n+1)}}. \tag{A4}$$

Next, considering only the first-order transmission and reflection coefficient inside each layer and after some straightforward calculations, a simplified expression of the Green's function with the observation point in n^{th} layer and the source point in 0th layer can be obtained as

$$G^{(n0)}(\vec{r}_r, \vec{r}_t) = \frac{1}{\pi} \int_{-\infty}^{+\infty} \frac{1}{k_{z0}}$$
$$\times \left[\prod_{q=0}^{n-1} \tilde{T}_{q(q+1)}^{\text{TM}} e^{-j\left[k_{zn}(z-d_0-\sum_{q=0}^{n-1} t_q) + \sum_{q=0}^{n-1} k_{zq}t_q \right]} + \right.$$
$$\left. \prod_{q=0}^{n-1} \tilde{R}_{q(q+1)}^{\text{TM}} \tilde{T}_{q(q+1)}^{\text{TM}} e^{+j\left[k_{zn}(z-d_0-\sum_{q=0}^{n-1} t_q) + \sum_{q=0}^{n-1} k_{zq}t_q \right]} \right]$$
$$\times e^{-jk_y(y-y_t)} dk_y. \tag{A5}$$

The Green's function in the preceding equation can be written as a summations of the transmitted and reflected terms, i.e., $G^{(n0)} = G_{\text{eb,T}}^{(n0)} + G_{\text{eb,R}}^{(n0)}$. In the following we address transmitted part and derive a closed-form for the Green's function of the multilayer media. Using the SPA [38], the first term in (A5) reduces as:

$$G_{\text{eb,T}}^{(n0)} = \frac{1}{\pi} \left(\prod_{q=0}^{n-1} \tilde{T}_{q(q+1)}^{\text{TM}}(k_{y,sp}) \right) \left[\frac{2\pi}{|\Phi_T''(k_{y,sp})|} \right]^{\frac{1}{2}}$$
$$\times e^{-j\left[k_{y,sp}(y-y_t) + \tilde{k}_{zn}(z-d_0-\sum_{q=0}^{n-1} t_q) + \sum_{q=0}^{n-1} \tilde{k}_{zq}t_q \right]}$$
$$\times e^{-j(\frac{\beta}{2} - \frac{\pi}{4})}, \tag{A6}$$

where

$$\Phi_T''(k_{y,sp}) = -\frac{k_n^2}{k_{zn}^3} \left(z - d_0 - \sum_{l=0}^{n-1} t_q \right) + \sum_{q=0}^{n-1} \frac{k_q^2}{k_{zq}^3} t_q, \tag{A7}$$

$$\Phi_T''(k_{y,sp}) = |\Phi_T''(k_{y,sp})| e^{-j\beta}, \tag{A8}$$

where $k_{y,sp}$ is the stationary point and is the solution of the following equations

$$k_{y,sp_1} = \frac{y - y_t}{\sum_{q=0}^{n-1} \frac{t_q}{k_{zq}} + \frac{1}{k_{zn}} \left(z - d_0 - \sum_{q=0}^{n-1} t_q \right)}, \tag{A9}$$

$$\tilde{k}_{zn} = \sqrt{k_n^2 - k_{y,sp}^2}. \tag{A10}$$

In Fig. 2, we compared FEM results with those of our asymptotic solution for frequencies $8\,\text{GHz}$ and $12\,\text{GHz}$. Here, the Green's function results are validated for a case of a point source in zeroth layer and observation point in first layer. The point source is located at $10\,\text{cm}$ distances to the top interface and observation points are at the middle of the first layer i.e., $z = 0\,\text{cm}$ and $-25\,\text{cm} \leq y \leq 25\,\text{cm}$. Result depicts that our developed asymptotic solution is well matched with the FEM solution.

APPENDIX B
HALF-SPACE FORMULATION

For the half-space case, the following terms can be represented as

$$\phi''(\bar{k}_y) = -\frac{k_1^2}{k_0} \left(\frac{1}{\bar{k}_{z1}^3} + \frac{1}{\bar{k}_{z1}'^3} \right) \left(1 - \frac{t_0}{z} \right) - k_0 \left(\frac{1}{\bar{k}_{z0}^3} + \frac{1}{\bar{k}_{z0}'^3} \right), \tag{B1}$$

and $\bar{k}_y$ is the solution of the following equation:

$$(y_t - y_r) + \left(-\frac{\bar{k}_y}{k_{z1}} + \frac{k_y'' - \bar{k}_y}{k_{z1}'} \right)(z - t_0) +$$
$$\left(-\frac{\bar{k}_y}{k_{z0}} + \frac{k_y'' - \bar{k}_y}{k_{z0}'} \right) t_0 = 0. \tag{B2}$$

The Green's function of the half-space can be simplified as follow where only the transmission part is employed

$$G_{\text{eb,T}}^{(10)} = \frac{1}{\pi} \left(\frac{2k_{z0}}{k_{z0} + k_{z1}} \right) \left[\frac{2\pi}{|\Phi_T''(k_{y,sp_1})|} \right]^{\frac{1}{2}}$$
$$\times e^{-j\left[k_{y,sp_1}(y-y_t) + \tilde{k}_{z1}d_1 + \tilde{k}_{z0}t_0 \right]} \times e^{-j(\frac{\beta}{2} - \frac{\pi}{4})}, \tag{B3}$$

$$k_{y,sp_1} \approx k_{z1} \frac{y - y_t}{z - d_1}. \qquad (B4)$$

Using these expressions, the object function O_1 and related calculations for moisture level estimation can be derived.

REFERENCES

[1] Z. Wu and H. Wang, "Microwave tomography for industrial process imaging: Example applications and experimental results.," *IEEE Antennas and Propagation Magazine*, vol. 59, pp. 61–71, Oct 2017.

[2] J. A. Tobon Vasquez, R. Scapaticci, G. Turvani, M. Ricci, L. Farina, A. Litman, M. R. Casu, L. Crocco, and F. Vipiana, "Noninvasive inline food inspection via microwave imaging technology: An application example in the food industry," *IEEE Antennas and Propagation Magazine*, vol. 62, no. 5, pp. 18–32, 2020.

[3] F. Becker, C. Schwabig, J. Krause, S. Leuchs, C. Krebs, R. Gruna, A. Kuter, T. Langle, D. Nuessler, and J. Beyerer, "From visual spectrum to millimeter wave: A broad spectrum of solutions for food inspection," *IEEE Antennas and Propagation Magazine*, vol. 62, no. 5, pp. 55–63, 2020.

[4] Y. Sun, *Adaptive and Intelligent Temperature Control of Microwave Heating Systems with Multiple Sources*. PhD thesis, KIT Scientific Publishing, Karlsruhe, 2016.

[5] A. C. Metaxas, *Industrial Microwave Heating*. Power and Energy, Institution of Engineering and Technology, 1988.

[6] Y. V. Bykov, K. I. Rybakov, and V. E. Semenov, "High-temperature microwave processing of materials," *Journal of Physics D: Applied Physics*, vol. 34, pp. R55–R75, jun 2001.

[7] A. Omrani, R. Yadav, M. Vauhkonen, G. Link, T. Lähivaara, and J. Jelonnek, "A combined microwave imaging algorithm for localization and moisture level estimation in multilayered media," in *2021 15th European Conference on Antennas and Propagation (EuCAP)*, pp. 1–5, 2021.

[8] R. Yadav, A. Omrani, M. Vauhkonen, G. Link, and T. Lähivaara, "Microwave tomography for moisture level estimation using Bayesian framework," in *2021 15th European Conference on Antennas and Propagation (EuCAP)*, pp. 1–5, 2021.

[9] D. Colton and R. Kress, *Inverse Acoustic and Electromagnetic Scattering Theory*. Berlin, Germany:Springer-Verlag, 1998.

[10] K. Ren and R. J. Burkholder, "A uniform diffraction tomographic imaging algorithm for near-field microwave scanning through stratified media," *IEEE Transactions on Antennas and Propagation*, vol. 64, no. 12, pp. 5198–5207, 2016.

[11] S. Sadeghi, K. Mohammadpour-Aghdam, R. Faraji-Dana, and R. J. Burkholder, "A DORT-uniform diffraction tomography algorithm for through-the-wall imaging," *IEEE Transactions on Antennas and Propagation*, vol. 68, no. 4, pp. 3176–3183, 2020.

[12] M. Kazemi, Z. Kavehvash, and M. Shabany, "K-space analysis of aliasing in millimeter-wave imaging systems," *IEEE Transactions on Microwave Theory and Techniques*, vol. 69, no. 3, pp. 1965–1973, 2021.

[13] M. Kazemi, Z. Kavehvash, and M. Shabany, "K-space aware multi-static millimeter-wave imaging," *IEEE Transactions on Image Processing*, vol. 28, no. 7, pp. 3613–3623, 2019.

[14] Y. Álvarez, Y. Rodriguez-Vaqueiro, B. Gonzalez-Valdes, F. Las-Heras, and A. García-Pino, "Fourier-based imaging for subsampled multistatic arrays," *IEEE Transactions on Antennas and Propagation*, vol. 64, no. 6, pp. 2557–2562, 2016.

[15] A. Omrani, G. Link, and J. Jelonnek, "A multistatic uniform diffraction tomographic algorithm for real-time moisture detection," in *2020 IEEE Asia-Pacific Microwave Conference (APMC)*, pp. 437–439, 2020.

[16] D. M. Sheen, "Sparse multi-static arrays for near-field millimeter-wave imaging," in *2013 IEEE Global Conference on Signal and Information Processing*, pp. 699–702, 2013.

[17] R. Yadav, A. Omrani, G. Link, M. Vauhkonen, and T. Lähivaara, "Microwave tomography using neural networks for its application in an industrial microwave drying system," *Sensors*, vol. 21, no. 20, 2021.

[18] R. Yadav, A. Omrani, G. Link, M. Vauhkonen, and T. Lähivaara, "Correlated sample-based prior in Bayesian inversion framework for microwave tomography," *IEEE Transactions on Antennas and Propagation*, pp. 1–1, 2022.

[19] A. Omrani, R. Yadav, G. Link, and J. Jelonnek, "A time-reversal imaging algorithm for localization and moisture level detection in the polymer foam in an industrial microwave drying system," in *AMPERE 2021 Proceedings*, Chalmers University of Technology (Chalmers), 2021. 38.03.02; LK 01.

[20] A. Omrani, M. Moghadasi, and M. Dehmollaian, "Localisation and permittivity extraction of an embedded cylinder using decomposition of the time reversal operator," *IET Microwaves, Antennas Propagation*, vol. 14, pp. 851–859(8), July 2020.

[21] A. Omrani, R. Yadav, G. Link, T. Lähivaara, M. Vauhkonen, and J. Jelonnek, "An electromagnetic time-reversal imaging algorithm for moisture detection in polymer foam in an industrial microwave drying system," *Sensors*, vol. 21, no. 21, 2021.

[22] C. T. Tai, *Dyadic Green's functions in electromagnetic theory*. IEEE Press, 1994.

[23] P. Zhang, X. Zhang, and G. Fang, "Comparison of the imaging resolutions of time reversal and back-projection algorithms in em inverse scattering," *IEEE Geoscience and Remote Sensing Letters*, vol. 10, no. 2, pp. 357–361, 2013.

[24] S. M. Moghadasi, M. Dehmollaian, and J. Rashed-Mohassel, "Time reversal imaging of deeply buried targets under moderately rough surfaces using approximate transmitted fields," *IEEE Transactions on Geoscience and Remote Sensing*, vol. 53, no. 7, pp. 3897–3905, 2015.

[25] W. C. Chew, *Waves and Fields in Inhomogenous Media*. IEEE Press, 1995.

[26] G. Lockwood, P.-C. Li, M. O'Donnell, and F. Foster, "Optimizing the radiation pattern of sparse periodic linear arrays," *IEEE Transactions on Ultrasonics, Ferroelectrics, and Frequency Control*, vol. 43, no. 1, pp. 7–14, 1996.

[27] S. M. Gehlbach and R. E. Alvarez, "Digital ultrasound imaging techniques using vector sampling and raster line reconstruction," *Ultrasonic Imaging*, vol. 3, no. 1, pp. 83–107, 1981. PMID: 7195096.

[28] S. S. Ahmed, A. Schiessl, F. Gumbmann, M. Tiebout, S. Methfessel, and L.-P. Schmidt, "Advanced microwave imaging," *IEEE Microwave Magazine*, vol. 13, no. 6, pp. 26–43, 2012.

[29] S. Soldatov, T. Kayser, G. Link, T. Seitz, S. Layer, and J. Jelonnek, "Microwave cavity perturbation technique for high-temperature dielectric measurements," in *2013 IEEE MTT-S International Microwave Symposium Digest (MTT)*, pp. 1–4, 2013.

[30] S. Sadeghi, K. Mohammadpour-Aghdam, R. Faraji-Dana, and R. J. Burkholder, "A novel algorithm for wall characterization in through the wall imaging based on spectral analysis," in *2018 18th International Symposium on Antenna Technology and Applied Electromagnetics (AN-TEM)*, pp. 1–2, 2018.

[31] S. Sadeghi, K. Mohammadpour-Aghdam, K. Ren, R. Faraji-Dana, and R. J. Burkholder, "A pole-extraction algorithm for wall characterization in through-the-wall imaging systems," *IEEE Transactions on Antennas and Propagation*, vol. 67, no. 11, pp. 7106–7113, 2019.

[32] H.-O. Peitgen and D. Saupe, eds., *The Science of Fractal Images*. Berlin, Heidelberg: Springer-Verlag, 1988.

[33] C. Moss, F. Teixeira, Y. Yang, and J. A. Kong, "Finite-difference time-domain simulation of scattering from objects in continuous random media," *IEEE Transactions on Geoscience and Remote Sensing*, vol. 40, no. 1, pp. 178–186, 2002.

[34] M. E. Yavuz and F. L. Teixeira, "On the sensitivity of time-reversal imaging techniques to model perturbations," *IEEE Transactions on Antennas and Propagation*, vol. 56, no. 3, pp. 834–843, 2008.

[35] L. Tsang and J. A. Kong, *Scattering of Electromagnetic Waves: Advanced Topics*. John Wiley & Sons, Ltd, 2001.

[36] M. E. Yavuz and F. L. Teixeira, "Space–frequency ultrawideband time-reversal imaging," *IEEE Transactions on Geoscience and Remote Sensing*, vol. 46, no. 4, pp. 1115–1124, 2008.

[37] Y. Zhang, A. Omrani, R. Yadav, and M. Fjeld, "Supporting visualization analysis in industrial process tomography by using augmented reality—a case study of an industrial microwave drying system," *Sensors*, vol. 21, no. 19, 2021.

[38] W. Chew, "A quick way to approximate a Sommerfeld-Weyl-type integral (antenna far-field radiation)," *IEEE Transactions on Antennas and Propagation*, vol. 36, no. 11, pp. 1654–1657, 1988.

Adel Omrani was born in Iran in 1991. He received the B.Sc. degree in electrical engineering from the University of Babol, Babol, in 2014, and the M.Sc. degree in electrical engineering from the University of Tehran, Tehran, Iran, in 2017. He is currently pursuing the Ph.D. degree in electrical engineering and information technology with the Karlsruhe Institute of Technology (KIT), Karlsruhe, Germany.
His current research interests include microwave imaging, antennas, numerical methods in electromagnetics, applied electromagnetic, and microwave engineering.

Rahul Yadav received his M.E. degree in electronics and communication engineering with a specialization in microwave engineering from the Birla Institute of Technology, Ranchi, India, in 2014, and is currently working toward the Ph.D. degree in the Department of Applied Physics, University of Eastern Finland, Kuopio, Finland. His Ph.D. research involves the development of fast reconstruction algorithms for microwave tomography for industrial applications. His research interests include computational electromagnetics, inverse problems, statistical signal processing, and monolithic microwave integrated circuits.

Guido Link received the Dipl.-Phys. and Dr. rer. nat. degree in physics from the Technical University Karlsruhe, Germany in 1990 and 1993, respectively. His diploma thesis and graduate research was devoted to the frequency and temperature dependent dielectric characterization of low loss ceramics and ionic crystals. Since 1993, he has been working at the Karlsruhe Institute of Technology, Germany (former Forschungszentrum Karlsruhe) in the field of high power microwave and millimeter-wave processing of materials as a team leader at the Institute for Pulsed Power and Microwave Technology. His research interest includes dielectric measurements, design and simulation of microwave systems and processes, microwave assisted sintering, curing of polymer composites, additive manufacturing, plasma chemistry. He authored or coauthored more than 200 contributed papers to international scientific conference and more than 30 papers in scientific journal and holds 8 patents.

John Jelonnek received the Dipl.-Ing. and Dr.-Ing. degrees in electrical engineering from Hamburg University of Technology (TUHH), Germany, in 1991 and 2000, respectively. At TUHH he developed rigorous self-consistent analyses for gyrotron oscillators with particular focus on rigorous time-domain simulation at mismatched conditions and injection locking. From 1997 to 2011, John Jelonnek was working in several different positions in industry. Since 2011, John Jelonnek is the Director of the Institute for Pulsed Power and Microwave Technology (IHM) at Karlsruhe Institute of Technology (KIT), Germany. Both, research and development of high-power microwave sources, with particular focus on megawatt-class gyrotrons, and applications of microwaves to energy efficient industrial processes using dielectric heating and microwave plasmas are in the focus. John Jelonnek is a Professor for high-power microwave technologies at KIT.